Hygroscopic Aerosols Amplify Longwave Downward Radiation in the Arctic

Denghui Ji[1,*], Mathias Palm[1], Matthias Buschmann[1], Kerstin Ebell[2], Marion Maturilli[3], Xiaoyu Sun[1], and Justus Notholt[1]

[1]Institute of Environmental Physics, University of Bremen, Otto-Hahn-Allee 1, 28359 Bremen, Germany
[2]Institute for Geophysics and Meteorology, University of Cologne, Zülpicher Str. 49a, DE-50674 Cologne, Germany
[3]Alfred Wegener Institute, Helmholtz Centre for Polar and Marine Research, Telegrafenberg A43, 14473 Potsdam, Germany

Correspondence: Denghui Ji (denghui_ji@iup.physik.uni-bremen.de)

Abstract. This study investigates the impact of hygroscopic aerosols, such as sea salt and sulfate, on longwave downward radiation in the Arctic. These aerosols absorb atmospheric water vapor, leading to wet growth, increased size, and enhanced longwave downward radiation emission, defined as the Aerosol Infrared Radiation Effect. Observations of aerosols, especially their composition, are challenging during the Arctic winter. We use an emission Fourier Transform Spectrometer to measure aerosol composition. Observations show that the Aerosol Infrared Radiation Effect of dry aerosols is limited to about 1.45 ± 2.00 Wm^{-2}. Wet growth significantly increases this effect. During winter, at relative humidity levels between 60% and 80%, wet aerosols exhibit effects approximately 7 times greater than dry aerosols. When relative humidity exceeds 80%, the effect can be up to 20 times higher. Sea salt aerosols in Ny-Ålesund demonstrate high effect values, while non-hygroscopic aerosols like black carbon and dust show consistently low values. Reanalysis data indicates increased water vapor and sea salt aerosol optical depth in Ny-Ålesund after 2000, correlating with significant positive temperature anomalies in this area. Besides, wet aerosols can remain activated even in dry environments, continuously contributing high effects, thereby expanding the area affected by aerosol-induced warming. This warming effect may exacerbate Arctic warming, acting as a positive feedback mechanism.

1 Introduction

Arctic amplification, characterized by the accelerated warming of the Arctic region compared to global averages, is a phenomenon of importance in climate change (Serreze and Barry, 2011; Wendisch et al., 2017; Peace et al., 2020). This amplified warming is particularly pronounced during the polar night, highlighting the need for a comprehensive understanding of its causes and consequences (Chung et al., 2021). To elucidate the underlying mechanisms driving Arctic amplification, extensive research has focused on key processes such as temperature feedback, surface albedo feedback, and cloud and water vapor feedback (Bony et al., 2006; Soden and Held, 2006; Graversen et al., 2014; Taylor et al., 2013; Philipp et al., 2020). Among these, aerosols are an important factor in Arctic climate dynamics, influencing various feedback mechanisms. For instance, dust and

Black Carbon (BC) deposition on snow or ice surfaces reduce albedo, accelerating ice melt (Ming et al., 2009; Bond et al., 2013). Moreover, sea salt aerosols modify cloud properties, enhancing longwave downward radiation (LWD) and contributing to surface warming (Gong et al., 2023).

25   In the context of the Arctic energy budget, LWD constitutes a critical component, primarily governed by greenhouse gases (GHGs) in the global mean (Trenberth et al., 2009; Wild et al., 2015; Tian et al., 2023). However, during the polar night when solar shortwave radiation is absent, the cooling effect of clouds and aerosols, arising from the scattering of solar radiation, becomes negligible (Cox et al., 2015). Therefore, LWD from clouds and aerosols assumes greater significance, particularly in maintaining the Arctic energy balance (Serreze and Barry, 2011; Cox et al., 2015; Lenaerts et al., 2017; Ebell et al., 2020).

30 Compared with LWD from clouds (50 - 100 Wm^{-2} (Serreze and Barry, 2011; Cox et al., 2015; Lenaerts et al., 2017; Ebell et al., 2020)), previous studies show that the LWD caused by aerosols in dry condition is usually lower than 10 Wm^{-2} (Spänkuch et al., 2000; Markowicz et al., 2003; Vogelmann et al., 2003; Lohmann et al., 2010). Dry aerosol particles contribute very limited LWD to the Arctic climate. However, LWD in the transition state (wet aerosols) between dry aerosols and cloud droplets is rarely mentioned.

35   Aerosols in the atmosphere, including sea salt and sulfates, possess hygroscopic properties, allowing them to absorb water vapor and undergo wet growth (Winkler, 1973). This process, known as aerosol wet growth, is accompanied by an increase in LWD (Mauritsen et al., 2011). The magnitude of this increase is influenced by factors such as aerosol composition, and ambient relative humidity (RH) (Peng et al., 2022). Notably, the deliquescence point, at which hygroscopic aerosols abruptly increase in size, is a critical threshold determined by ambient RH (Tang and Munkelwitz, 1993; Winkler, 1973). For example,

40 the sea salt and sulfate aerosols in this study have deliquescence points of about 75% and 85%, respectively (Peng et al., 2022). This means that when the ambient humidity increases to 75%, the dry sea salt aerosol particles can absorb water vapor in the atmosphere and become larger. If the ambient humidity continues to increase, the sea salt wet particles will continue to absorb water and become sea salt solution droplets (still belonging to aerosols). This is the wet growth process of sea salt aerosols. Recent studies have shown an increase in Arctic water vapor content, attributed to enhanced poleward transport facilitated by

45 atmospheric river pathways (Sato et al., 2022; Thandlam et al., 2022; Bresson et al., 2022; Lauer et al., 2023). Moreover, sea salt aerosols have been identified as dominant contributors to Arctic aerosol composition during the winter season (Huang and Jaeglé, 2017; Kirpes et al., 2018). Therefore, the rise in coarse-mode aerosols, primarily originating from sea spray, and the increase of RH in the Arctic underscore the need to investigate the potential impact of aerosols on LWD and Arctic warming during their wet growth process (Heslin-Rees et al., 2020; Pernov et al., 2022).

50   Given the complex interplay between aerosols (especially aerosol composition), RH, and LWD, understanding the radiative effects of aerosol wet growth is crucial for understanding the role of aerosols in Arctic amplification, particularly during the polar night. Considering the various factors contributing to atmospheric LWD, such as greenhouse gases, clouds, and aerosols, this study aims to explore the extra LWD introduced during aerosol wet growth. Thus, we focuses on hygroscopic aerosols, particularly sea salt and sulfate aerosols. Our study focuses on humidity levels below 100%, meaning we only discuss aerosols

55 in their dry and wet states. We take aerosol in RH < 60% as dry states. When the environment becomes more humid (RH > 60%), a hygroscopic particle can absorb water, and its size grows, which can act as cloud condensation nuclei (CCN). This

hygroscopic particle is defined as wet aerosol in our study. To achieve this, both model simulations and observational data (Site location: Ny-Ålesund; Time period: Dec-Jan-Fer, 2017 - 2022) will be utilized, defining the resulting additional LWD from aerosols as the Aerosol Infrared Radiation Effect (ARE). This paper is structured as follows: Section 3 provides an overview

60 of the datasets utilized, including Fourier-transform infrared spectroscopy (FTIR) and Baseline Surface Radiation Network (BSRN) measurements. Section 4 outlines the methodologies employed to derive ARE from LWD measurements (eliminating contributions from clouds and GHGs) in detail. The results are presented in Section 5. Finally, the implications of these findings are discussed in the conclusion section 7.

2   Site Description

65   Ny-Ålesund (78.925 °N, 11.925 °E), Svalbard, is located in the North Atlantic atmospheric transport gateway to the Arctic. It serves as a central hub for international Arctic research, attracting scientists from around the world to study various environmental and climate-related phenomena, in particular to monitor Arctic amplification. The region stretching from Svalbard to the Barents and Kara Seas is currently experiencing particularly intense winter warming, with temperatures rising by more than +3 K per decade (Dahlke and Maturilli, 2017). This region is also an important pathway for air mass transport between

70   the Arctic and mid-latitudes (Graßl et al., 2022). Today, Ny-Ålesund is primarily a research town, hosting several year-round research stations operated by different nations. Key activities focus on long-term atmospheric monitoring, studying the effects of climate change in the Arctic, and tracking the transport of pollutants and aerosols from lower latitudes to the Arctic. Due to its location and concentration of research infrastructure, Ny-Ålesund is a well-known site for Arctic research, providing invaluable data and insights into one of the most rapidly changing regions on Earth.

75   3   Data

All observations and model simulations in this study are conducted in Ny-Ålesund. The surface radiation measurements, radiosonde launches, and all measurements by cloud radar, microwave radiometer, ceilometer, and FTIR, are operated at the Atmosphere Observatory of the AWIPEV research base that is run jointly by the German Alfred Wegener Institute, and the French Polar Institute. Data from both observations are filtered by using Cloudnet data to ensure cloud-free conditions, focusing

80   solely on aerosols.

The FTIR plays a crucial role in elucidating the relationship between aerosol composition and ARE, offering detailed insights into aerosol composition while quantifying ARE. However, the ARE from the FTIR is restricted to the atmospheric window region (AW, 690 - 1390 cm^{-1}; 7 - 14 µm). On the other hand, the BSRN provides LWD data across the entire mid-infrared region (4.5 - 42 µm) but cannot characterize aerosol composition. Each dataset presents different advantages and limitations.

85   Furthermore, it is essential to account for the influences of other radiative sources, such as clouds and greenhouse gases, to accurately assess ARE.

3.1 Clouds and Aerosols Signals from Cloudnet

In order to identify cloud cases, the Cloudnet classification product is used (Illingworth et al., 2007). Cloudnet is operationally applied to the AWIPEV measurement (Nomokonova et al., 2019; Ebell et al., 2023). Within the Cloudnet processing, information from a cloud radar, ceilometer, microwave radiometer and output from a numerical weather prediction model is combined and the backscattered signals by the radar and ceilometer are classified in terms of the occurrence of "Aerosol & insects", "Insects", "Aerosols", "Melting & droplets", "Ice & droplets", "Ice", "Drizzle & droplets", "Drizzle or rain" and "Droplets". The classification profiles have a vertical resolution of 20 m and extend from 120 m to about 11 km height above the surface. The Cloudnet data used in this study are measured from 2017 to 2022, with temporal resolution of 30s. The application of this data to the FTIR and BSRN is slightly different, and the specific methods are given in the respective sections (Sec.4.1 for FTIR and Sec.4.4 for BSRN).

3.2 LWD in Atmospheric Window Measured from FTIR

A Fourier Transform spectrometer, called NYAEM-FTS, for measuring down-welling emission in the thermal infrared was installed in Ny-Ålesund in the summer of 2019. The NYAEM-FTS consists of a Bruker Vertex 80 Fourier Transform Spectrometer, an SR800 blackbody, an automatically operated gold mirror to select the radiation source, and an automatically operated hutch which shields the instrument from the environment. It is situated in a temperature-stabilized laboratory, at about 21 - 25 °C. The beamsplitter is a KBr beam splitter and the detector is an extended Mercury Cadmium Telluride (MCT) detector.

Therefore, the infrared spectra are measured by FTIR. Since the infrared emission of aerosols is primarily concentrated in the atmospheric window (Ji et al., 2023), integrating the spectrum within this region provides the longwave radiation (LWD) data from the FTIR. The FTIR spectra used in this study are measured from 2019 to 2022. More details on the emission FTIR can be found in Ji et al. (2023). The methods used to obtain the ARE from measured spectra are presented in Sec.4.1.

3.3 Aerosol Composition Data from FTIR

Since aerosol composition should also be considered during the aerosol wet growth process, it is worthwhile to study the ARE with different aerosol compositions. Ji et al. (2023) have shown previously that the aerosol composition (sulfate, sea salt, dust, and BC) can be retrieved from emission FTIR using the retrieval algorithm, called the second version of Total Cloud Water RETrieval (TCWRET-V2; TCWRET-V1 is developed by Richter et al. (2022) for cloud retrieval.). In this retrieval algorithm, the meteorological data are used and taken from ERA5 hourly data on pressure levels (Hersbach et al., 2023). In this study, the look-up tables of aerosol optical properties required for the retrieval algorithm have been updated, including the wet growth process of aerosols. Following the method described in Ji et al. (2023), sulfate (dry or wet state), sea salt (dry or wet state), dust, and BC are retrieved under different RH conditions. The retrieved aerosol composition data are from 2019 to 2022. Further details on how to retrieve aerosol composition considering aerosol wet growth are given in Sec.4.3.

3.4 LWD in Mid-infrared Range from BSRN

The radiation measurements (the LWD) are from Maturilli (2020) at station Ny-Ålesund. The Baseline Surface Radiation
120   Network (BSRN) is a global network of high-quality ground-based stations established to observe amongst others the upward
and downward long-wave radiation. All data are quality-controlled. LWD (4.5 - 42 μm) measurements from BSRN are expected
to have an uncertainty within ± 5 $\mathrm{Wm^{-2}}$ (Maturilli et al., 2015). The LWD data used in this study are measured in every winter
(December-January-February, DJF) from 2017 to 2022, with a temporal resolution of 1 min.

3.5 Water vapor Profiles from Radiosonde

125   As we mentioned before, LWD measured by BSRN includes the emitted radiation of GHGs, clouds, and aerosols. Cloud
cases can be identified by Cloudnet, while the contribution from GHGs should also be considered. The vertical profiles of
temperature, pressure, and RH (water vapor) are used from the radiosonde measurements (Maturilli and Dünschede, 2023).
The Alfred Wegener Institute (AWI) has been performing radiosonde measurements at Ny-Ålesund since 1991, with regular
daily 12 UTC launches since 1992. In order to extend this existing homogenized data record, the 2017 to 2022 Ny-Ålesund
130   radiosonde data processed by the Global Climate Observing System (GCOS) Reference Upper-Air Network (GRUAN) have
been interpolated on the according height resolution. The combined uncertainty given by the manufacturer is 4% for RH. The
duration for the radiosonde ascent profile from the surface to 30 km is about 90 minutes. The radiosonde data in this study are
measured in every winter (DJF) from 2017 to 2022, with temporal resolution of 1d.

3.6 Reanalysis Datasets

135   This study uses two reanalysis datasets, one from European Centre for Medium-Range Weather Forecasts (ECMWF) Reanal-
ysis v5 (ERA5) and the other from Modern-Era Retrospective analysis for Research and Applications version 2 (MERRA-2).
The RH and temperature data are from ERA5 monthly averaged data on pressure levels (900 hPa) from 1980 to 2022 (Hersbach
et al., 2023).

   The sea salt aerosol AOD data is derived from monthly MERRA-2 datasets (single level) (Gelaro et al., 2017). MERRA-
140   2 is the latest version of global atmospheric reanalysis for the satellite era produced by the NASA Global Modeling and
Assimilation Office (GMAO) using the Goddard Earth Observing System Model (GEOS) version 5.12.4. The dataset covers
the period of 1980-present. Aerosols in MERRA-2 are simulated with a radiatively coupled version of the Goddard Chemistry,
Aerosol, Radiation, and Transport model (GOCART). GOCART treats the sources, sinks, and chemistry of 15 externally mixed
aerosol mass mixing ratio tracers, including sea salt (Randles et al., 2017).

4 Methods

4.1 AREₐw from FTIR

The downwelling radiance emitted by the atmosphere, including aerosols or clouds, can be measured using FTIR. For Emission FTIR, the waveband that is sensitive to aerosols is the atmospheric window region. To distinguish the LWD and ARE measured by FTIR (7 - 14 μm) from the later mentioned LWD and ARE from BSRN (4.5 - 42 μm), here we use the subscript 'AW' to denote the quantity measured by the FTIR. Note that AW is only part of the mid-infrared band of BSRN, so the radiation measured by FTIR is not comparable to the radiation measured by BSRN. Additionally, in the atmospheric window, the contribution from greenhouse gases (GHGs) is much smaller than that from clouds or aerosols, making the cloud signal the only factor that needs to be considered. Considering the small field of view (FOV) of the FTIR instrument (3.3 mrad), we excluded any data with cloud signals were detected within 30 minutes before or after the observation time. This method ensures that the FTIR's FOV remains cloud-free during the analysis. Specifically, when Cloudnet (Ebell et al., 2023) indicates an aerosol-only signal in the total atmospheric column, the spectra from the FTIR observations for that period will be used, while spectra from other periods will be discarded. As Cloudnet provides aerosol height information, the RH at the aerosol layer is obtained from ERA5 hourly data on pressure levels (Hersbach et al., 2023), with the error of RH about 2% (Gamage et al., 2020).

In order to calculate AREₐw, the radiance measured by emission FTIR has to be first considered to the broadband LWD_{AW}. The ARE in the atmosphere window is given by:

$$ARE_{AW} = LWD_{AW} - LWD_{AW\_clean} \tag{1}$$

where LWD_{AW} is the calculated LWD in AW range with the measurements of emission spectra by FTIR; LWD_{AW_clean} is the emission flux from a clean atmosphere (no clouds and no aerosols), which can be calculated using the LBLDIS model (Line-By-Line Radiative Transfer Model coupled with DIScrete Ordinates Radiative Transfer Model, and details of this model are given in the Sec.4.2.) or observed by FTIR under the ideal conditions of an environment without aerosols and clouds. Here, LBLDIS model simulations under a clean sky are used. The temperature, water vapor, and pressure profiles from ERA5 are used in LBLDIS as input files, other GHGs are fixed in the model. The equation for LWD_{AW}, from the spectral radiance I (in $Wm^{-2}cm^{-1}sr^{-1}$) is given as follows:

$$LWD_{AW} = \iiint I(v,\mu,\phi)\mu d\mu d\phi dv \tag{2}$$

where I is the radiance, μ is the cosine of the zenith angle, ϕ is the azimuthal angle, and v is the wave number. Integrating the radiance over both the hemisphere and the wave number yields the LWD_{AW}. The wave number for AW ranges from 690 to $1390\,cm^{-1}$ (7 - 14 μm) (Cox et al., 2015). Similar to the method used in Cox et al. (2012), the relationship between radiance and LWD_{AW} is calculated using an exponential function assumption of radiance dependence on μ , as follows:

$$\int_{690cm^{-1}}^{1390cm^{-1}} I(v,\mu)dv = \int_{690cm^{-1}}^{1390cm^{-1}} I(v,\mu=1) \cdot (a \cdot e^{-b\cdot\mu} + c)dv \tag{3}$$

where a, b, and c are the fitted coefficients, given by the LBLDIS. For a more concise expression, we here abbreviate the wave number integral of radiance $\int_{690cm^{-1}}^{1390cm^{-1}} I(v, \mu = 1)dv$ as II_{AW}. Therefore, the final flux calculation function could be written as follows:

$$
\begin{aligned}
\text{LWD}_{\text{AW}} &= C \cdot \pi \cdot II_{\text{AW}}, \\
C &= 2 \cdot \int_0^1 (a \cdot e^{-b \cdot \mu} + c)\mu d\mu.
\end{aligned}
\tag{4}
$$

C is the correction coefficient for non-isotropic emissions, which is variable for different emissions, such as aerosols, atmosphere in clear day and thin clouds. This correction coefficient C has been determined by LBLDIS model simulations and a value of 1.35 ±0.05 for aerosols in the atmospheric window. The method of how to get this correction coefficient is given in Appendix A.

The error of spectra measured by FTIR is usually less than 1 $\text{mWm}^{-2}\text{cm}^{-1}\text{sr}^{-1}$ in AW region (Ji et al., 2023), the uncertainty of the correction coefficient for non-isotropic emission from aerosol is about $\pm$ 0.05 here, therefore, the theoretical error of LWD_{AW} from FTIR is $\sqrt{\left(\frac{\partial \text{LWD}_{\text{AW}}}{\partial II_{\text{AW}}} \cdot \Delta II_{\text{AW}}\right)^2 + \left((\frac{\partial \text{LWD}_{\text{AW}}}{\partial C} \cdot \Delta C)\right)^2}$, about 0.550 Wm^{-2}.

4.2 ARE_{AW} from LBLDIS Model Simulation

To analyze the key parameters affecting the aerosol infrared radiation, we perform model simulations also in the atmospheric window. Considering model simulation of downwelling emission from the atmosphere, two radiative transfer models are coupled and used in this case, one is the Line-by-Line Radiative Transfer Model (LBLRTM) (Clough et al., 2005) for the gaseous contribution, another is the DIScrete Ordinate Radiative Transfer model (DISORT) (Stamnes et al., 1988) for calculation of water droplets and aerosol particles. The coupled model is called LBLDIS (Turner, 2005). This radiative transfer model is also used as a forward model in the aerosol composition retrieval algorithm described in Ji et al. (2023). The software of the retrieval algorithm is also public available (see section "data availability").

The ARE_{AW} calculation method from simulated spectra using the LBLDIS model is similar to the method mentioned in Sec.4.1. The only difference in this section is that additional aerosol information is added to LBLDIS to get the model simulated ARE_{AW}. ARE of two aerosols, sea salt and sulfate (Ammonium sulfate), are simulated by radiative transfer model (LBLDIS). Since the model setups for sea salt and sulfate are similar, only the parameters in the model for sea salt are described in detail here. Usually, aerosol sizes in the Arctic region are often below 1 μm, according to the measurements of aerosol size distribution in the Arctic (Asmi et al., 2016; Park et al., 2020; Boyer et al., 2022). Weinbruch et al. (2012) found that sea salt particles were most abundant in particles larger than 0.5 μm. Therefore, in dry conditions, it is assumed that the size of sea salt is fixed at 1 μm and has the shape of a sphere. The aerosol size distribution is assumed to be a uniform distribution. All aerosols are fixed at a height of 1000 meters above the ground. Several model simulations are run under various RH conditions (65% as dry condition, 75% - 95% as wet conditions), with various aerosol number densities (50 cm^{-3} - 5000 cm^{-3}). As for sulfate, the size is assumed to be smaller, 0.4 μm in model simulations in dry conditions, and other settings are the same as those for the sea salt case. The input data for LBLDIS includes profiles of temperature, pressure, and humidity, which are sourced from ERA5 (Hersbach et al., 2023).

4.3 Aerosol Composition Retrieval from Emission FTIR

Ji et al. (2023) describe a modified retrieval algorithm for retrieving aerosol composition. The primary difference in different versions of the retrieval algorithm are the scattering properties look-up tables for various emission sources, such as clouds (Richter et al., 2022) or dry (Ji et al., 2023) or activated aerosols (in this study). For activated aerosols, look-up tables are updated for sea salt and sulfate following the steps described in Ji et al. (2023). An additional step in creating a new look-up table of activated aerosols is to consider the complex refractive index of wet aerosols and the particle size of hygroscopic particles as a function of relative humidity. Therefore, the following parameterization method (Zieger et al., 2013; Petters and Kreidenweis, 2007) is applied:

$$\frac{r_{wet}(RH)}{r_{dry}} = \left(1 + \kappa \frac{RH}{1 - RH}\right)^{1/3} \tag{5}$$

where r_{wet} is the radius of wet aerosols; r_{dry} is the radius of dry aerosols; κ is the hygroscopic growth parameter of the aerosols.

To calculate the complex refractive index ($R_{wet} + i \cdot I_{wet}$) of wet aerosol, the volume fraction of dry aerosol (Chin et al., 2002), f_d, is used:

$$\begin{cases} R_{wet} = & f_d R_d + (1 - f_d) R_{water} \\ I_{wet} = & f_d I_d + (1 - f_d) I_{water} \end{cases} \tag{6}$$

where R_d and R_{water} mean the real part of the refractive index of dry particles and water respectively; I_d and I_{water} mean the imaginary part respectively.

4.4 ARE in the Mid-infrared Range from BSRN

The measurement of LWD (4.5 - 42 μm) from the atmosphere is obtained from the BSRN. Since we are only focusing on the ARE in cloud-free cases in this study, cloud-free conditions should be filtered and radiation from greenhouse gases (GHGs) should be eliminated by the combination of BSRN measurements and radiative transfer simulation based on clean-sky radiosonde data, as follows:

1. Firstly, with the help of the Cloudnet dataset, the LWD measured by BSRN during cloud-free periods is selected, called LWD_aero-only. Within the altitude range (0 − 12 km) of the "Classification" product of Cloudnet (see Sec.3.1), an aerosol-only situation is selected when only "Aerosols" are present in all of the above targets. Then observations of the BSRN are selected that correspond to these times, resulting in aerosol-only BSRN observations. Note that, the LWD from BSRN is the downward radiation of the entire hemispheric atmosphere. This means that simply being cloud-free vertically is not enough to ensure that the entire sky is cloud-free. Therefore, the cloud-free period is ensured to 3 hours around 12:00 (10:30 to 13:30). Besides, during this time period, the radiosonde profile measurement starts at around 11:00 and lasts for about 90 minutes.

2. Water vapor, the most important greenhouse gas (GHG), contributes more significantly to LWD relative to other GHGs (Easterbrook, 2016). Therefore, the next step is to subtract the contribution of water vapor to LWD:

$$ARE = LWD_{aerosol\text{-}only} - LWD_{clean} \tag{7}$$

where LWD_{clean} means the infrared radiation flux of clean sky (no clouds and no aerosols), which is given by the radiative transfer model simulation. Since LBLDIS is mainly used in the AW region, the radiative transfer model used to calculate LWD_{clean} in mid-infrared range is the SBDART (Santa Barbara DISORT Atmospheric Radiative Transfer, (Ricchiazzi et al., 1998)). Water vapor profiles, pressure, and temperature profiles are from sounding data, other GHGs are fixed to SBDART defaults.

3. Based on the water vapor profiles, we classify the ARE into four scenarios based on the difference in the line shape of the RH profiles: ARE_{dry}, $ARE_{surface}$, $ARE_{intrusion}$ and $ARE_{multilayer}$. ARE_{dry} means that the entire atmosphere is in a dry state (RH < 60%); $ARE_{surface}$ means that there is a layer of high humidity (RH > 60%) near the ground (< 1 km); $ARE_{intrusion}$ represents the situation with a layer of high humidity intrusion (RH > 60%) at high altitude (> 1 km). $ARE_{multilayer}$ is the case that the atmosphere has multiple layers of high humidity (RH > 60%) and not used in this study.

Note that the time resolution of the $LWD_{aero\text{-}only}$ data is 1 minute, while the time resolution of the sounding profiles is once per day (launched at 11:00 UTC), with each ground to high altitude (about 30 km, maximum height the balloon can reach) observation period lasting about 90 minutes (the sonde needs about 30 minutes to cross the troposphere). Therefore, the $LWD_{aero\text{-}only}$ measurements are averaged over the time period (10:30 UTC - 13:30 UTC) to represent the ARE at 12:00 UTC. Besides, we also consider the possibility that cloud contamination might persist despite the absence of detectable clouds within the 180-minute window before and after 12:00 UTC. To address this consideration, an additional criterion is implemented: data are flagged as cloud-contaminated if cloud signals were detected outside this 180-minute window. The aerosol radiative effect calculations from this cloud-contaminated data are excluded from ARE. This enhanced screening method ensures that the remaining dataset represents cloud-free sky conditions.

In addition, RH is a key parameter in the aerosol wet growth process and no additional data is indicating at which altitude hygroscopic aerosols are located. On one hand, air masses from the mid-latitudes transport both moisture and aerosols to the Arctic. On the other hand, aerosols are dispersed throughout the atmosphere and become activated at particular altitudes where the relative humidity reaches their deliquescence point. Therefore, we assume here that the peaks in each RH profile are the RH of the activated aerosols. All in all, a total of 100 cases were available after these filter methods were carried out. These cases were divided into four types: 15 cases in ARE_{dry}, 41 cases in $ARE_{surface}$, 5 cases in $ARE_{intrusion}$, and 39 cases in $ARE_{multilayer}$. It is important to note that when there are several peaks of high RH in the atmospheric water vapor profile (here is two peaks in this study), it is challenging to precisely determine the exact layer in which the aerosol resides. To avoid introducing excessive uncertainty, the results for these cases, $ARE_{multilayer}$, are not included in the results.

Since radiosonde profile measurements are conducted once daily, using the observed atmospheric data to represent conditions between 10:30 and 13:30 may introduce some errors. To assess the uncertainty in the LWD due to daily variations in water

270   vapor, we conducted model simulations. These simulations varied only the water vapor column content while keeping other atmospheric parameters constant, as depicted in Fig. B1. Assuming the profile accurately represents the atmospheric state for half of the time in Ny-Ålesund, while the other half is characterized by subpolar conditions. This assumption results in an LWD effect of approximately 2.8 $\mathrm{Wm^{-2}}$. Therefore, it is reasonable to approximate atmospheric conditions during this three-hour window using the once-daily radiosonde profile observations.

275 ## 5   Results

5.1   Warming Effect of Aerosols during Wet Growth

When examining the relationship between $\mathrm{ARE_{AW}}$ and RH in the model simulation (Sec.4.2), as shown in Fig.1a, a sharp increase in $\mathrm{ARE_{AW}}$ is predicted as RH rises. This abrupt enhancement in $\mathrm{ARE_{AW}}$ corresponds to the aerosol's deliquescence point. Specifically, the transition point of $\mathrm{ARE_{AW}}$ is mainly determined by aerosol composition. For example, the $\mathrm{ARE_{AW}}$

280   associated with sea salt aerosols, characterized by a number density of 500 $\mathrm{cm^{-3}}$ (depicted as the solid black line in Fig. 1a), suddenly increases to 7 $\mathrm{Wm^{-2}}$ at an RH level of 75%, which is about 7 times higher than that in dry conditions (about 1 $\mathrm{Wm^{-2}}$). The magnitude of this number concentration (500 $\mathrm{cm^{-3}}$) is within the measurable range at NY-Ålesund (Jung et al., 2018; Pasquier et al., 2022). In contrast, sulfate aerosols exhibit the transition point of $\mathrm{ARE_{AW}}$ at 85% as the deliquescence RH of sulfate values at 85% (Peng et al., 2022) (indicated by the dashed black line in Fig. 1a).

285   Figure 1b depicts the $\mathrm{ARE_{AW}}$ measurements under varying ambient RH (Cloudnet is used to determine the altitude at which the aerosol was located, and then the RH value for that altitude is obtained from the ERA5.) conditions for different dominant aerosol composition in Ny-Ålesund based on FTIR measurements. When the dominant aerosol is sea salt and sulfate, the $\mathrm{ARE_{AW}}$ from the FTIR observation also increases as RH rises. The corresponding RH of sudden enhancement of $\mathrm{ARE_{AW}}$ in sea salt dominated cases is about 80% - 85%, while that in sulfate dominated cases is around 90%. Based on FTIR observations,

290   the aerosol composition is primarily dominated by sea salt, with sulfate playing a secondary role. Moreover, the FTIR observations align closely with model simulations (sea salt case with a number concentration of 500 $\mathrm{cm^{-3}}$). Both observations and simulations show that during the early stages of aerosol wet growth (75% < RH < 80%), the aerosol infrared radiative effect increases from approximately $1 - 2$ $\mathrm{Wm^{-2}}$ to 10 $\mathrm{Wm^{-2}}$. Subsequently, as RH approaches 90%, the ARE reaches about 20 $\mathrm{Wm^{-2}}$. Conversely, for non-hygroscopic aerosols, such as dust and black carbon, the $\mathrm{ARE_{AW}}$ is about 1.45 ± 2.00 $\mathrm{Wm^{-2}}$ and

295   does not change with RH, which is close to previous studies (Spänkuch et al., 2000; Markowicz et al., 2003; Vogelmann et al., 2003; Lohmann et al., 2010).

BSRN measurements give the ARE in the mid-infrared range, as shown in Fig.1c. The analysis in Fig.1c considers the ARE in three distinct scenarios: $\mathrm{ARE_{dry}}$, $\mathrm{ARE_{surface}}$, and $\mathrm{ARE_{intrusion}}$, each representing single-layer high RH scenarios based on water vapor profiles from radiosonde (methods see sec.4.4). Overall, we observe the trending that ARE increases with rising

300   RH. Specifically, under dry conditions (RH < 60%), the ARE remains a low value of about 2.1 ± 3.7 $\mathrm{Wm^{-2}}$ and does not vary with RH, which is consistent with previous findings (see Fig.1a and b). As RH increases to between 60% and 80%, the ARE shows a significant increase. Specifically, in the cases of $\mathrm{ARE_{surface}}$, the mean ARE averaged between 60% to 80% RH

is approximately 14.9 ± 8.5 Wm^{-2}. Besides, in all five ARE$_{intrusion}$ scenario cases, there are three cases of high water vapor intrusion, but the values of ARE does not increase with RH, and only other two cases show an enhancement of ARE at 70% RH. It's important to note that even under very high ambient humidity conditions (RH > 90%), we still observe low ARE values, which is due to the presence of non-hygroscopic aerosols (dust or BC) from FTIR measurements. Furthermore, within high RH conditions (RH > 90%), there are no intermediate ARE values, with transitions primarily occurring within the RH range of 70% to 80%. This indicates that prevalent hygroscopic aerosols in Ny-Ålesund undergo a transformation from a dry to a wet state within this RH range.

Notably, we differentiate the potential radiative effect from the cloud contamination. In Fig.1c, when RH is 60% - 80%, the infrared radiative effect from aerosol only (orange and blue dots) can be about 20 Wm^{-2}, which is comparable with the infrared radiative effect combined aerosol with potential cloud contamination (gray dots). However, when the environment becomes more humid (RH > 80%), differentiating the radiative effect between cloud and aerosol is challenging due to the observation method. This implies that the estimation of ARE with RH less than 80% is more reliable than that of RH>80%.

5.2   RH Temperature and Sea Salt AOD Changes in the Arctic

To depict the humidity conditions in the Arctic, Figure 2a presents the difference of RH between 2000 - 2022 and 1980 - 2000 in the Arctic at 900 hPa in winter (DJF). In the region around Ny-Ålesund, RH has significantly increased, showing a rise of approximately 2 - 6% compared to pre-2000 levels. Typically, as Arctic warming, rising temperatures often lead to a decrease in RH. However, the notable increase in RH at Ny-Ålesund suggests that specific humidity is increasing more rapidly in this region compared to other parts of the Arctic. This anomaly points to unique local atmospheric conditions or processes that are enhancing moisture content more effectively than elsewhere in the Arctic.

MERRA2 reanalysis data, illustrated in Figure 2b, indicate a general decrease in sea salt AOD across the Arctic compared to the pre-2000 period. However, there is a notable increase in sea salt AOD in Ny-Ålesund and nearby area. The difference in sea salt AOD between 2000-2022 and 1980-2000 reveals a statistically significant positive anomaly near Ny-Ålesund, approximately +0.005.

When combining the changes in RH and sea salt AOD anomaly, we observe that regions with high humidity and positive sea salt AOD anomalies coincide with areas experiencing large positive temperature anomalies, as shown in Figure 2c. Specifically, these regions exhibit temperature anomalies around +3 ^{o}C. These findings highlight the significant role of aerosol wet growth in the Arctic. The suitable RH conditions in Ny-Ålesund have likely facilitated the wet growth of sea salt aerosols, contributing to the observed positive temperature anomalies.

6   Discussion

FTIR and BSRN observations are operating on different spectral bands—FTIR focusing on the atmospheric window spectrum region and BSRN covering a broader infrared spectrum. It is worth noting that the estimations of the absolute radiation value from two observation methods are not comparable because of the different spectrum range. However, if the cross-validation

of these methods is needed, we can roughly compare them in terms of how many times they have grown in radiation from dry to wet aerosol. Both FTIR and BSRN observations consistently indicate that within the relative humidity range of 60% – 80%, aerosol wet growth results in an approximate 7 times increase in ARE compared to dry conditions. At high humidity (> 80%), the FTIR instrument can capture the infrared radiative enhancement by aerosol wet growth because of the small field of view (FOV = 3.3 mrad). In contrast, BSRN all-sky observation, which requires a completely cloud-free sky across the entire observation domain, are more susceptible to cloud contamination under high-humidity conditions. As a result, BSRN is limited in providing precise ARE values at higher humidity levels. This distinction highlights the strengths and limitations of each observational method under different atmospheric conditions.

Our study shows that wet aerosols have an additional warming effect. However, when the relative humidity exceeds 80%, Cloudnet always observes some cloud signals during the period beyond the 180-minute window in BSRN measurements. We cannot conclusively determine whether high values of LWD ($> 40 \mathrm{Wm}^{-2}$) are solely caused by aerosols or are the result of cloud contamination (see Fig.1). Under the very humid conditions (RH > 80%), wet aerosols become activated and transform to cloud droplets. This phenomenon from BSRN observation aligns with our hypothesis, indicating that the observed ambient RH corresponds to the deliquescence point, such as 80% for sea salt (Peng et al., 2022). Given that the maximum ARE value for RH levels between 60% and 80% is approximately 36 Wm^{-2}, values exceeding this threshold may attribute to cloud droplets. The results of this study indicate that when an instrument is unable to differentiate between the particle sizes of aerosols and cloud droplets with sufficient accuracy, utilizing the ARE or LWD to distinguish between aerosols and clouds can be a potential method.

Based on the FTIR measurements and LBLDIS model simulations, RH and aerosol composition are the most important factors influencing ARE_{AW}. The measurement of aerosol composition, especially by remote sensing method, is still challenging. In this study, we applied an FTIR retrieval algorithm to retrieve an aerosol composition measurement for all RH conditions, which is a complement to the previous method in Ji et al. (2023). According to Ji et al. (2023), the larger the aerosol AOD, the stronger the aerosol composition signal and the more reliable the retrieved results. For example, in this study, in a case of a sea salt dominant event (compare in Fig.1b), as shown in Tab.1, the AOD of the sea salt is 0.1125 ± 0.0013, while that of dust aerosol in this case is 0.0128 ± 0.007. BC (0.0001 ± 0.0013) and sulfate aerosol (0.0001 ± 0.0109) are present during this event, however, their contribution is not the dominant factor. In other words, the error of the dominant aerosol composition in AOD retrieval is about 1.16%. Furthermore, as we analysed in sec.4.1, the error of ARE_{AW} measured by FTIR is about 0.550 Wm^{-2}, which is more accurate than that from BSRN (about 5 Wm^{-2}). Therefore, emission FTIR is a helpful instrument to do the aerosol composition and ARE measurements.

Several studies have shown that Arctic water vapor content is increasing, primarily due to enhanced poleward transport from mid-latitudes via atmospheric river pathways (Sato et al., 2022; Thandlam et al., 2022; Bresson et al., 2022; Lauer et al., 2023). ERA5 reanalysis data, as presented in the Fig.2a, indicates that Ny-Ålesund has high water vapor levels during winter, providing suitable ambient RH conditions for aerosol wet growth. MERRA-2 reanalysis data further reveals a positive anomaly in sea salt AOD in the area around Ny-Ålesund after 2000 (Fig.2b). Besides, numerous studies have indicated that during the winter season, sea salt aerosols can dominate the Arctic aerosol composition (Huang and Jaeglé, 2017; Kirpes et al., 2018).

370 Our results (Fig.1b) corroborate this, demonstrating that in scenarios dominated by sea salt aerosols, the infrared radiative effect is most pronounced in Ny-Ålesund. Kirpes et al. (2018) also affirm that sea salt constitutes the principal contributor to accumulation and coarse-mode aerosols during the Arctic winter. Heslin-Rees et al. (2020) have demonstrated that coarse mode aerosols, primarily originating from sea spray, have exhibited an increase over the last two decades (1999 – 2016) at the Zeppelin Observatory on Svalbard. This observed trend can be attributed predominantly to alterations in air mass circulation

375 patterns, with a higher frequency of air masses originating from the Northern Atlantic region (Pernov et al., 2022).

Our measurements, yielding high ARE of hygroscopic aerosols and very low ARE of non-hygroscopic aerosols, indicates sea salt aerosols are very import for the Arctic warming in winter. MERRA-2 reanalysis data, as shown in Fig. 3, confirms our results that in Ny-Ålesund, sea salt and sulfate aerosols are significantly dominant than other aerosol components in winter. As spring arrives, sea salt AOD begins to decline while dust AOD gradually increases. Arctic dust aerosol primarily originates

380 from natural sources such as desert regions, with approximately 65% from Africa (Sahara desert), 22% from Asian deserts, and 13% from other deserts (Kok et al., 2021; Breider et al., 2014). Arctic dust aerosol concentrations peak in spring when long-range transport from Africa and Asia is most efficient (Groot Zwaaftink et al., 2016). This trend continues into summer, when sea salt levels reach their lowest point. Given that sea salt is a major component of winter aerosols, its contribution to Arctic winter warming requires further investigation in the future.

385 Combining the changes in RH and the sea salt AOD anomaly, the region of high humidity with positive sea salt AOD anomalies overlaps the regions with the large positive temperature anomalies (see Fig.2c). Based on these findings, it is crucial to consider the warming effect of aerosols under high humidity conditions when studying Arctic amplification. The greenhouse effect of water vapor intensifies surface warming, leading to higher humidity levels in the Arctic (Beer and Eisenman, 2022), which facilitates aerosol wet growth. Increased aerosols in a wet state further warm the Arctic atmosphere, potentially leading

390 to more water vapor and creating a positive feedback loop in Arctic amplification. Therefore, studying the longwave radiation (LWD) contributions from both water vapor and aerosols together is essential.

Although the area of positive sea salt AOD anomalies is very limited in the Arctic, the differences in the deliquescence and efflorescence points during aerosol wet growth process can have the potential to expand the warming effect of aerosols throughout the whole polar regions. Wet aerosols can maintain their hydrated state until they either develop into cloud droplets

395 in supersaturated conditions or revert to dry particles in drier environments, typically below the efflorescence point (Lillard et al., 2009). For instance, as shown in Fig.4, sodium chloride (NaCl) has a deliquescence point of approximately 75% RH and an efflorescence point of around 46% RH (Peng et al., 2022). Consequently, NaCl remains in a wet state after activation (the black dashed line in Fig.4) until ambient RH drops below the efflorescence point (e.g. 45% RH). Therefore, the Ny-Ålesund region can act as a "refueling station" for the wet growth of the hygroscopic aerosols, specifically the sea salt aerosols,

400 resulting in a warming effect. Here, these aerosols are activated, and after leaving the region, they can remain activated and travel throughout the Arctic, carrying high values of ARE as long as the ambient humidity is higher than the efflorescence point.

7 Conclusions

In this study, based on the measurements from FTIR, BSRN, Cloudnet, and radiosonde, the infrared radiative effect of aerosols during the wet growth process has been investigated. Under dry conditions (RH < 60%), the ARE in the whole mid-infrared range remains to about 2.1 ± 3.7 Wm^{-2}. As RH increases, a significant increase in ARE is observed. Between RH levels of 60% and 80%, the average ARE is about 14.9 ± 8.5 Wm^{-2}, about 7 times than that of dry aerosols. Moreover, in cases where the aerosol layer becomes more humid (RH > 80%), according to FTIR measurement, the ARE can be further higher, about 20 times than that in dry state. Besides, the prevalent hygroscopic aerosol in Ny-Ålesund from FTIR measurements is sea salt, undergoing a transformation from a dry to a wet state within the RH range of 70% - 80%. The analysis of ERA5 data indicates that Ny-Ålesund has maintained RH levels above 80%, which are conducive to the wet growth of aerosols. MERRA2 reanalysis data shows a positive anomaly in sea salt AOD in this area, approximately + 0.005, compared to the pre-2000 period. Combining the RH and sea salt AOD, the study finds that areas with high humidity and increased sea salt AOD overlap with regions experiencing significant positive temperature anomalies. Furthermore, if aerosols are highly activated in Ny-Ålesund, they will remain activated after leaving the region as long as the ambient humidity is above the efflorescence point and will propagate throughout the Arctic with high values of ARE.

The results highlight the importance of aerosol wet growth in influencing Arctic climate. The high humidity in Ny-Ålesund as well as nearby area around Svalbard likely promotes the growth of sea salt aerosols, which in turn may contribute to warming through increased longwave downward radiation. These interactions are crucial for understanding Arctic amplification. Continuous monitoring and detailed analysis of these factors are essential for predicting future changes in the Arctic environment.

Data availability. All data used in this article are given in detail in sec. 2. Here we briefly illustrate the data. The Ny-Ålesund radiation measurements are available at the PANGAEA data repository at https://doi.org/10.1594/PANGAEA.914927 (Maturilli, 2020). Data from Cloudnet (https://cloudnet.fmi.fi/, Ebell et al. (2023)), a product named "Classification", is used to do aerosol-only case selection in BSRN data. The homogenized radiosonde record obtained is made available at https://doi.org/10.1594/PANGAEA.961203 (Maturilli and Dünschede, 2023). The latest version of TCWret (the retrieval algorithm for FTIR), including LBLDIS download instructions, can be downloaded from Zenodo (https://doi.org/10.5281/zenodo.3948048, Richter et al. (2022)). The ERA5 data used in Fig.2 a and c is from Hersbach et al. (2023). Sea salt AOD data from MERRA-2 can be download at https://disc.gsfc.nasa.gov/datasets/M2TMNXAER_5.12.4/summary (Gelaro et al., 2017).

Appendix A: Non-isotropic emissions correction coefficient

The relationship between integral calculation of radiance in the AW region, II_{AW}, with the cosine of the zenith angle, μ, is assumed as exponent. Figure A1 presents the relationship II_{AW} with μ. The integral of the fitted function with μ could be calculated as the correction coefficient in Equation 4 after getting the fitted function (black dotted lines), and the flux in the unit of Wm^{-2} could then be obtained. In this figure, the aerosol type is dry sea salt with a 1 μm (diameter). The method of

aerosol hygroscopic growth mentioned in Sec.4.3 is used to calculate the wet particles. The varied colors indicate the various number densities of sea salt, while the black line stands for a clear sky scenario. Four cases from the LBLDIS simulation at four RH conditions (65%, 75%, 85%, and 95%) are provided as well. When the aerosol number density is low, between 50 and 500 cm^{-3}, the ratio of $II_{AW}(\mu)$ to $II_{AW}(\mu = 1)$ at various u remains relatively constant. With a sharper relationship in dry conditions and a progressive flattening with an increase in RH, this phenomenon occurs in all RH cases. Furthermore, the differences in the equations at higher relative humidity levels (75%, 85%, and 95%) are not apparent, suggesting that the correction coefficient for non-isotropic aerosol scenarios may be similar under wet conditions. Additionally, such a relationship dramatically flattens as RH rises in the presence of heavy aerosol pollution, such as that present in the case of 5000 cm^{-3}, and tends to be isotropic in high RH as in the case of RH=95%. We anticipate that under high RH condition, a significant number of aerosols will progressively activate and develop into a thick cloud in the atmosphere that emits isotropic radiation.

Following the simulation of the sea salt, the sulfate aerosol is also calculated by LBLDIS. Table .A1 displays the whole results, including the atmosphere on a clear day. The correction coefficient for a clear atmosphere is approximately 1.08. For a clear sky, the light from atmosphere emission could be very nearly isotropic. While for aerosols, sea salt has a correction coefficient of 1.40 in dry state and roughly 1.35 in wet, which is considerably different from clear day. Although the activated RH for sulfate aerosol and sea salt is different (75% for sea salt and 85% for sulfate), both exhibit similar correction coefficient values when they are activated.

In conclusion, non-isotropic radiance emission from aerosols should be taken into account while doing flux calculation for a moderate aerosol event, which frequently occurs in the Arctic. In dry conditions, aerosols have a different correction coefficient than they do in wet conditions. It is not very varied for various aerosol types.

Author contributions. D.J., X.S., M.P.,M.B. and J.N. conceived and designed the study. D.J. collected, organized and processed data, developed the retrieval algorithm and write this paper. K.E. gave advice in LWD from water vapour and provided detailed descriptions of the Cloudnet data. M.M. gave advice in BSRN and sounding data. X.S. gave advice in model simulation, data processing and physical mechanism. M.P. and M.B designed and built the measurement setup, performed FTIR measurements and gave advice in the retrieval algorithm. J.N. gave advice in the article structure and the frame of the scientific content. All co-authors made contribution to the revision of this article.

Competing interests. The authors declare no competing interests.

Acknowledgements. We acknowledge ACTRIS and Finnish Meteorological Institute for providing the data set which is available for download from https://cloudnet.fmi.fi. The cloud radar data for Ny-Ålesund was provided by the University of Cologne, the ceilometer and microwave radiometer data by the Alfred Wegener Institute, Helmholtz Centre for Polar and Marine Research. We thank the staff of AWIPEV research base in Ny-Ålesund for technical support of the measurements. This work is funded by the AWIPEV research as part of the projects AWIPEV-0016, and the Deutsche Forschungsgemeinschaft (DFG, German Research Foundation) - project number 268020496

- TRR 172, within the "Transregional Collaborative Research Center 'ArctiC Amplification: Climate Relevant Atmospheric and SurfaCe

465   Processes, and Feedback Mechanisms (AC)3'". We acknowledge ECMWF for providing IFS model data, DWD for providing ICON model data, and NCEP (National Centers for Environmental Prediction) for providing access to GDAS1 data. We thank the AWI Bremerhaven and the AWI Potsdam for logistical support on the AWIPEV research base and the station personnel for on-site support. We thank the senate of Bremen for partial funding of this work.

References

470   Asmi, E., Kondratyev, V., Brus, D., Laurila, T., Lihavainen, H., Backman, J., Vakkari, V., Aurela, M., Hatakka, J., Viisanen, Y., Uttal, T., Ivakhov, V., and Makshtas, A.: Aerosol size distribution seasonal characteristics measured in Tiksi, Russian Arctic, Atmos. Chem. Phys., 16, 1271–1287, https://doi.org/10.5194/acp-16-1271-2016, 2016.

Beer, E. and Eisenman, I.: Revisiting the Role of the Water Vapor and Lapse Rate Feedbacks in the Arctic Amplification of Climate Change, Journal of Climate, 35, 2975 – 2988, https://doi.org/https://doi.org/10.1175/JCLI-D-21-0814.1, 2022.

475   Bond, T. C., Doherty, S. J., Fahey, D. W., Forster, P. M., Berntsen, T., DeAngelo, B. J., Flanner, M. G., Ghan, S., Kärcher, B., Koch, D., et al.: Bounding the role of black carbon in the climate system: A scientific assessment, J. Geophys. Res.: Atmos., 118, 5380–5552, https://doi.org/10.1002/jgrd.50171, 2013.

Bony, S., Colman, R., Kattsov, V. M., Allan, R. P., Bretherton, C. S., Dufresne, J.-L., Hall, A., Hallegatte, S., Holland, M. M., Ingram, W., Randall, D. A., Soden, B. J., Tselioudis, G., and Webb, M. J.: How Well Do We Understand and Evaluate Climate Change Feedback

480   Processes?, J. Clim., 19, 3445 – 3482, https://doi.org/10.1175/JCLI3819.1, 2006.

Boyer, M., Aliaga, D., Pernov, J. B., Angot, H., Quéléver, L. L. J., Dada, L., Heutte, B., Dall'Osto, M., Beddows, D. C. S., Brasseur, Z., Beck, I., Bucci, S., Duetsch, M., Stohl, A., Laurila, T., Asmi, E., Massling, A., Thomas, D. C., Nøjgaard, J. K., Chan, T., Sharma, S., Tunved, P., Krejci, R., Hansson, H. C., Kulmala, M., Petäjä, T., Sipilä, M., Schmale, J., and Jokinen, T.: A full year of aerosol size distribution data from the central Arctic under an extreme positive Arctic Oscillation: Insights from the MOSAiC expedition, Atmos. Chem. Phys.

485   Discuss., 2022, 1–45, https://doi.org/10.5194/acp-2022-591, 2022.

Breider, T. J., Mickley, L. J., Jacob, D. J., Wang, Q., Fisher, J. A., Chang, R. Y.-W., and Alexander, B.: Annual distributions and sources of Arctic aerosol components, aerosol optical depth, and aerosol absorption, Journal of Geophysical Research: Atmospheres, 119, 4107– 4124, https://doi.org/https://doi.org/10.1002/2013JD020996, 2014.

Bresson, H., Rinke, A., Mech, M., Reinert, D., Schemann, V., Ebell, K., Maturilli, M., Viceto, C., Gorodetskaya, I., and Crewell, S.: Case

490   study of a moisture intrusion over the Arctic with the ICOsahedral Non-hydrostatic (ICON) model: resolution dependence of its representation, Atmospheric Chemistry and Physics, 22, 173–196, https://doi.org/10.5194/acp-22-173-2022, 2022.

Chin, M., Ginoux, P., Kinne, S., Torres, O., Holben, B. N., Duncan, B. N., Martin, R. V., Logan, J. A., Higurashi, A., and Nakajima, T.: Tropospheric Aerosol Optical Thickness from the GOCART Model and Comparisons with Satellite and Sun Photometer Measurements, Journal of the Atmospheric Sciences, 59, 461 – 483, https://doi.org/https://doi.org/10.1175/1520-0469(2002)059<0461:TAOTFT>2.0.CO;2, 2002.

495   Chung, E.-S., Ha, K.-J., Timmermann, A., Stuecker, M. F., Bodai, T., and Lee, S.-K.: Cold-season Arctic amplification driven by Arctic ocean-mediated seasonal energy transfer, Earth's Future, 9, e2020EF001 898, https://doi.org/https://doi.org/10.1029/2020EF001898, 2021.

Clough, S., Shephard, M., Mlawer, E., Delamere, J., Iacono, M., Cady-Pereira, K., Boukabara, S., and Brown, P.: Atmospheric radiative transfer modeling: a summary of the AER codes, J. Quant. Spectrosc. Radiat. Transfer, 91, 233–244, https://doi.org/https://doi.org/10.1016/j.jqsrt.2004.05.058, 2005.

500   Cox, C. J., Walden, V. P., and Rowe, P. M.: A comparison of the atmospheric conditions at Eureka, Canada, and Barrow, Alaska (2006–2008), Journal of Geophysical Research: Atmospheres, 117, https://doi.org/https://doi.org/10.1029/2011JD017164, 2012.

Cox, C. J., Walden, V. P., Rowe, P. M., and Shupe, M. D.: Humidity trends imply increased sensitivity to clouds in a warming Arctic, Nature Communications, 6, 10 117, https://doi.org/10.1038/ncomms10117, 2015.

Dahlke, S. and Maturilli, M.: Contribution of Atmospheric Advection to the Amplified Winter Warming in the Arctic North Atlantic Region,

505   Advances in Meteorology, 2017, 4928 620, https://doi.org/https://doi.org/10.1155/2017/4928620, 2017.

Easterbrook, D.: Chapter 9 - Greenhouse Gases, in: Evidence-Based Climate Science (Second Edition), edited by Easterbrook, D. J., pp. 163–173, Elsevier, second edition edn., https://doi.org/https://doi.org/10.1016/B978-0-12-804588-6.00009-4, 2016.

Ebell, K., Nomokonova, T., Maturilli, M., and Ritter, C.: Radiative Effect of Clouds at Ny-Ålesund, Svalbard, as Inferred from Ground-Based Remote Sensing Observations, Journal of Applied Meteorology and Climatology, 59, 3 – 22, https://doi.org/10.1175/JAMC-D-19-0080.1, 2020.

Ebell, K., Maturilli, M., Ritter, C., and O'Connor, E.: Custom collection of classification data from Ny-Ålesund between 10 Jun 2016 and 31 Dec 2022, ACTRIS Cloud remote sensing data centre unit (CLU), https://doi.org/https://doi.org/10.60656/0f41eadb2ec84e4d, 2023.

Ebell, K., Schnitt, S., and Krobot, P.: Precipitation amount of Pluvio rain gauge at AWIPEV, Ny-Ålesund (2019), PANGAEA, https://doi.org/10.1594/PANGAEA.957615, in: Ebell, K et al. (2023): Precipitation amount of Pluvio rain gauge at AWIPEV, Ny-Ålesund (2017-2021). PANGAEA, https://doi.org/10.1594/PANGAEA.957612, 2023.

Gamage, S. M., Sica, R., Martucci, G., and Haefele, A.: A 1D var retrieval of relative humidity using the ERA5 dataset for the assimilation of Raman lidar measurements, Journal of Atmospheric and Oceanic Technology, 37, 2051–2064, https://doi.org/10.1175/JTECH-D-19-0170.1, 2020.

Gelaro, R., McCarty, W., Suárez, M. J., Todling, R., Molod, A., Takacs, L., Randles, C. A., Darmenov, A., Bosilovich, M. G., Reichle, R., Wargan, K., Coy, L., Cullather, R., Draper, C., Akella, S., Buchard, V., Conaty, A., da Silva, A. M., Gu, W., Kim, G.-K., Koster, R., Lucchesi, R., Merkova, D., Nielsen, J. E., Partyka, G., Pawson, S., Putman, W., Rienecker, M., Schubert, S. D., Sienkiewicz, M., and Zhao, B.: The Modern-Era Retrospective Analysis for Research and Applications, Version 2 (MERRA-2), J. Clim., 30, 5419 – 5454, https://doi.org/10.1175/JCLI-D-16-0758.1, 2017.

Gong, X., Zhang, J., Croft, B., Yang, X., Frey, M. M., Bergner, N., Chang, R. Y.-W., Creamean, J. M., Kuang, C., Martin, R. V., et al.: Arctic warming by abundant fine sea salt aerosols from blowing snow, Nature Geoscience, 16, 768–774, https://doi.org/10.1038/s41561-023-01254-8, 2023.

Graßl, S., Ritter, C., and Schulz, A.: The Nature of the Ny-Ålesund Wind Field Analysed by High-Resolution Windlidar Data, Remote Sensing, 14, https://doi.org/10.3390/rs14153771, 2022.

Graversen, R. G., Langen, P. L., and Mauritsen, T.: Polar Amplification in CCSM4: Contributions from the Lapse Rate and Surface Albedo Feedbacks, J. Clim., 27, 4433 – 4450, https://doi.org/10.1175/JCLI-D-13-00551.1, 2014.

Groot Zwaaftink, C. D., Grythe, H., Skov, H., and Stohl, A.: Substantial contribution of northern high-latitude sources to mineral dust in the Arctic, J. Geophys. Res.: Atmos., 121, 13,678–13,697, https://doi.org/https://doi.org/10.1002/2016JD025482, 2016.

Hersbach, H., Bell, B., Berrisford, P., Biavati, G., Horányi, A., Muñoz Sabater, J., Nicolas, J., Peubey, C., Radu, R., Rozum, I., Schepers, D., Simmons, A., Soci, C., Dee, D., and Thépaut, J.-N.: ERA5 monthly mean data on pressure levels from 1940 to present, Copernicus climate change service (c3s) climate data store (cds). (Accessed on < 01-12-2022 >), 10, https://doi.org/10.24381/cds.6860a573, 2023.

Heslin-Rees, D., Burgos, M., Hansson, H.-C., Krejci, R., Ström, J., Tunved, P., and Zieger, P.: From a polar to a marine environment: has the changing Arctic led to a shift in aerosol light scattering properties?, Atmospheric Chemistry and Physics, 20, 13 671–13 686, https://doi.org/10.5194/acp-20-13671-2020, 2020.

Huang, J. and Jaeglé, L.: Wintertime enhancements of sea salt aerosol in polar regions consistent with a sea ice source from blowing snow, Atmospheric Chemistry and Physics, 17, 3699–3712, https://doi.org/10.5194/acp-17-3699-2017, 2017.

Illingworth, A., Hogan, R., O'connor, E., Bouniol, D., Brooks, M., Delanoë, J., Donovan, D., Eastment, J., Gaussiat, N., Goddard, J., et al.: Cloudnet: Continuous evaluation of cloud profiles in seven operational models using ground-based observations, Bulletin of the American Meteorological Society, 88, 883–898, https://doi.org/https://doi.org/10.1175/BAMS-88-6-883, 2007.

Ji, D., Palm, M., Ritter, C., Richter, P., Sun, X., Buschmann, M., and Notholt, J.: Ground-based remote sensing of aerosol proper-

545   ties using high-resolution infrared emission and lidar observations in the High Arctic., Atmospheric Measurement Techniques, 16, https://doi.org/10.5194/amt-16-1865-2023, 2023.

Jung, C. H., Yoon, Y. J., Kang, H. J., Gim, Y., Lee, B. Y., Ström, J., Krejci, R., and Tunved, P.: The seasonal characteristics of cloud condensation nuclei (CCN) in the arctic lower troposphere, Tellus B: Chemical and Physical Meteorology, https://doi.org/10.1080/16000889.2018.1513291, 2018.

550 Kirpes, R. M., Bondy, A. L., Bonanno, D., Moffet, R. C., Wang, B., Laskin, A., Ault, A. P., and Pratt, K. A.: Secondary sulfate is internally mixed with sea spray aerosol and organic aerosol in the winter Arctic, Atmospheric Chemistry and Physics, 18, 3937–3949, https://doi.org/10.5194/acp-18-3937-2018, 2018.

Kok, J. F., Adebiyi, A. A., Albani, S., Balkanski, Y., Checa-Garcia, R., Chin, M., Colarco, P. R., Hamilton, D. S., Huang, Y., Ito, A., Klose, M., Li, L., Mahowald, N. M., Miller, R. L., Obiso, V., Pérez García-Pando, C., Rocha-Lima, A., and Wan, J. S.: Contribu-

555   tion of the world's main dust source regions to the global cycle of desert dust, Atmospheric Chemistry and Physics, 21, 8169–8193, https://doi.org/10.5194/acp-21-8169-2021, 2021.

Lauer, M., Rinke, A., Gorodetskaya, I., Sprenger, M., Mech, M., and Crewell, S.: Influence of atmospheric rivers and associated weather systems on precipitation in the Arctic, EGUsphere, 2023, 1–32, https://doi.org/10.5194/egusphere-2023-261, 2023.

Lenaerts, J. T., Van Tricht, K., Lhermitte, S., and L'Ecuyer, T. S.: Polar clouds and radiation in satellite observations, reanalyses, and climate

560   models, Geophysical Research Letters, 44, 3355–3364, https://doi.org/https://doi.org/10.1002/2016GL072242, 2017.

Lillard, R. S., Kolman, D. G., Hill, M. A., Prime, M. B., Veirs, D. K., Worl, L. A., and Zapp, P.: Assessment of Corrosion-Based Failure in Stainless Steel Containers Used for the Long-Term Storage of Plutonium-Based Salts, Corrosion, 65, 175–186, https://doi.org/10.5006/1.3319126, 2009.

Lohmann, U., Rotstayn, L., Storelvmo, T., Jones, A., Menon, S., Quaas, J., Ekman, A. M., Koch, D., and Ruedy, R.: Total aerosol effect:

565   radiative forcing or radiative flux perturbation?, Atmospheric Chemistry and Physics, 10, 3235–3246, https://doi.org/10.5194/acp-10-3235-2010, 2010.

Markowicz, K. M., Flatau, P. J., Vogelmann, A. M., Quinn, P. K., and Welton, E. J.: Clear-sky infrared aerosol radiative forcing at the surface and the top of the atmosphere, Quarterly Journal of the Royal Meteorological Society, 129, 2927–2947, https://doi.org/https://doi.org/10.1256/qj.02.224, 2003.

570 Maturilli, M.: Basic and other measurements of radiation at station Ny-Ålesund (2006-05 et seq), https://doi.org/10.1594/PANGAEA.914927, 2020.

Maturilli, M. and Dünschede, E.: Homogenized radiosonde record at station Ny-Ålesund, Spitsbergen, 2017-2022, https://doi.org/10.1594/PANGAEA.961203, 2023.

Maturilli, M., Herber, A., and König-Langlo, G.: Surface radiation climatology for Ny-Ålesund, Svalbard (78.9 N), basic observations for

575   trend detection, Theoretical and Applied Climatology, 120, 331–339, https://doi.org/10.1007/s00704-014-1173-4, 2015.

Mauritsen, T., Sedlar, J., Tjernström, M., Leck, C., Martin, M., Shupe, M., Sjogren, S., Sierau, B., Persson, P., Brooks, I., et al.: An Arctic CCN-limited cloud-aerosol regime, Atmospheric Chemistry and Physics, 11, 165–173, https://doi.org/10.5194/acp-11-165-2011, 2011.

Ming, J., Xiao, C., Cachier, H., Qin, D., Qin, X., Li, Z., and Pu, J.: Black Carbon (BC) in the snow of glaciers in west China and its potential effects on albedos, Atmos. Res., 92, 114–123, https://doi.org/https://doi.org/10.1016/j.atmosres.2008.09.007, 2009.

580 Nomokonova, T., Ritter, C., and Ebell, K.: HATPRO microwave radiometer measurements at AWIPEV, Ny-Ålesund (2016-2018), https://doi.org/10.1594/PANGAEA.902183, 2019.

Pałm, M., Melsheimer, C., Noël, S., Heise, S., Notholt, J., Burrows, J., and Schrems, O.: Integrated water vapor above Ny Ålesund, Spitsbergen: a multi-sensor intercomparison, Atmospheric Chemistry and Physics, 10, 1215–1226, https://doi.org/10.5194/acp-10-1215-2010, 2010.

585 Park, J., Dall'Osto, M., Park, K., Gim, Y., Kang, H. J., Jang, E., Park, K.-T., Park, M., Yum, S. S., Jung, J., Lee, B. Y., and Yoon, Y. J.: Shipborne observations reveal contrasting Arctic marine, Arctic terrestrial and Pacific marine aerosol properties, Atmos. Chem. Phys., 20, 5573–5590, https://doi.org/10.5194/acp-20-5573-2020, 2020.

Pasquier, J. T., David, R. O., Freitas, G., Gierens, R., Gramlich, Y., Haslett, S., Li, G., Schäfer, B., Siegel, K., Wieder, J., Adachi, K., Belosi, F., Carlsen, T., Decesari, S., Ebell, K., Gilardoni, S., Gysel-Beer, M., Henneberger, J., Inoue, J., Kanji, Z. A., Koike, M., Kondo, Y., Krejci, 590 R., Lohmann, U., Maturilli, M., Mazzolla, M., Modini, R., Mohr, C., Motos, G., Nenes, A., Nicosia, A., Ohata, S., Paglione, M., Park, S., Pileci, R. E., Ramelli, F., Rinaldi, M., Ritter, C., Sato, K., Storelvmo, T., Tobo, Y., Traversi, R., Viola, A., and Zieger, P.: The Ny-Ålesund Aerosol Cloud Experiment (NASCENT): Overview and First Results, Bulletin of the American Meteorological Society, 103, E2533 – E2558, https://doi.org/10.1175/BAMS-D-21-0034.1, 2022.

Peace, A., Carslaw, K., Lee, L., Regayre, L., Booth, B., Johnson, J., and Bernie, D.: Effect of aerosol radiative forcing uncertainty on 595 projected exceedance year of a 1.5° C global temperature rise, Environmental Research Letters, 15, 0940a6, https://doi.org/10.1088/1748-9326/aba20c, 2020.

Peng, C., Chen, L., and Tang, M.: A database for deliquescence and efflorescence relative humidities of compounds with atmospheric relevance, Fundamental Research, 2, 578–587, https://doi.org/https://doi.org/10.1016/j.fmre.2021.11.021, 2022.

Pernov, J. B., Beddows, D., Thomas, D. C., Dall´ Osto, M., Harrison, R. M., Schmale, J., Skov, H., and Massling, A.: Increased aerosol 600 concentrations in the High Arctic attributable to changing atmospheric transport patterns, npj Climate and Atmospheric Science, 5, 62, https://doi.org/10.1038/s41612-022-00286-y, 2022.

Petters, M. D. and Kreidenweis, S. M.: A single parameter representation of hygroscopic growth and cloud condensation nucleus activity, Atmospheric Chemistry and Physics, 7, 1961–1971, https://doi.org/10.5194/acp-7-1961-2007, 2007.

Philipp, D., Stengel, M., and Ahrens, B.: Analyzing the Arctic Feedback Mechanism between Sea Ice and Low-Level Clouds Using 34 Years 605 of Satellite Observations, J. Clim., 33, 7479 – 7501, https://doi.org/10.1175/JCLI-D-19-0895.1, 2020.

Randles, C. A., da Silva, A. M., Buchard, V., Colarco, P. R., Darmenov, A., Govindaraju, R., Smirnov, A., Holben, B., Ferrare, R., Hair, J., Shinozuka, Y., and Flynn, C. J.: The MERRA-2 Aerosol Reanalysis, 1980 Onward. Part I: System Description and Data Assimilation Evaluation, Journal of Climate, 30, 6823 – 6850, https://doi.org/10.1175/JCLI-D-16-0609.1, 2017.

Ricchiazzi, P., Yang, S., Gautier, C., and Sowle, D.: SBDART: A Research and Teaching Software Tool for Plane-Parallel Radiative Transfer 610 in the Earth's Atmosphere, Bulletin of the American Meteorological Society, 79, 2101 – 2114, https://doi.org/https://doi.org/10.1175/1520-0477(1998)079<2101:SARATS>2.0.CO;2, 1998.

Richter, P., Palm, M., Weinzierl, C., Griesche, H., Rowe, P. M., and Notholt, J.: A dataset of microphysical cloud parameters, retrieved from Fourier-transform infrared (FTIR) emission spectra measured in Arctic summer 2017, Earth Syst. Sci. Data, 14, 2767–2784, https://doi.org/10.5194/essd-14-2767-2022, 2022.

615 Sato, T., Nakamura, T., Iijima, Y., and Hiyama, T.: Enhanced Arctic moisture transport toward Siberia in autumn revealed by tagged moisture transport model experiment, npj Climate and Atmospheric Science, 5, 91, https://doi.org/10.1038/s41612-022-00310-1, 2022.

Serreze, M. C. and Barry, R. G.: Processes and impacts of Arctic amplification: A research synthesis, Global and Planetary Change, 77, 85–96, https://doi.org/https://doi.org/10.1016/j.gloplacha.2011.03.004, 2011.

Soden, B. J. and Held, I. M.: An Assessment of Climate Feedbacks in Coupled Ocean–Atmosphere Models, J. Clim., 19, 3354 – 3360, https://doi.org/10.1175/JCLI3799.1, 2006.

Spänkuch, D., Döhler, W., and Güldner, J.: Effect of coarse biogenic aerosol on downwelling infrared flux at the surface, Journal of Geophysical Research: Atmospheres, 105, 17 341–17 350, https://doi.org/https://doi.org/10.1029/2000JD900173, 2000.

Stamnes, K., Tsay, S.-C., Wiscombe, W., and Jayaweera, K.: Numerically stable algorithm for discrete-ordinate-method radiative transfer in multiple scattering and emitting layered media, Appl. Opt., 27, 2502–2509, https://doi.org/10.1364/AO.27.002502, 1988.

Tang, I. N. and Munkelwitz, H. R.: Composition and temperature dependence of the deliquescence properties of hygroscopic aerosols, Atmospheric Environment. Part A. General Topics, 27, 467–473, https://doi.org/https://doi.org/10.1016/0960-1686(93)90204-C, 1993.

Taylor, P. C., Cai, M., Hu, A., Meehl, J., Washington, W., and Zhang, G. J.: A Decomposition of Feedback Contributions to Polar Warming Amplification, J. Clim., 26, 7023 – 7043, https://doi.org/10.1175/JCLI-D-12-00696.1, 2013.

Thandlam, V., Rutgersson, A., and Sahlee, E.: Spatio-temporal variability of atmospheric rivers and associated atmospheric parameters in the Euro-Atlantic region, Theoretical and Applied Climatology, pp. 1–21, https://doi.org/10.1007/s00704-021-03776-w, 2022.

Tian, Y., Zhong, D., Ghausi, S. A., Wang, G., and Kleidon, A.: Understanding variations in downwelling longwave radiation using Brutsaert's equation, Earth System Dynamics, 14, 1363–1374, https://doi.org/10.5194/esd-14-1363-2023, 2023.

Trenberth, K. E., Fasullo, J. T., and Kiehl, J.: Earth's Global Energy Budget, Bulletin of the American Meteorological Society, 90, 311 – 324, https://doi.org/10.1175/2008BAMS2634.1, 2009.

Turner, D. D.: Arctic Mixed-Phase Cloud Properties from AERI Lidar Observations: Algorithm and Results from SHEBA, J. Appl. Meteorol., 44, 427 – 444, https://doi.org/10.1175/JAM2208.1, 2005.

Vogelmann, A. M., Flatau, P. J., Szczodrak, M., Markowicz, K. M., and Minnett, P. J.: Observations of large aerosol infrared forcing at the surface, Geophysical research letters, 30, https://doi.org/https://doi.org/10.1029/2002GL016829, 2003.

Weinbruch, S., Wiesemann, D., Ebert, M., Schütze, K., Kallenborn, R., and Ström, J.: Chemical composition and sources of aerosol particles at Zeppelin Mountain (Ny Ålesund, Svalbard): An electron microscopy study, Atmospheric Environment, 49, 142–150, https://doi.org/https://doi.org/10.1016/j.atmosenv.2011.12.008, 2012.

Wendisch, M., Brückner, M., Burrows, J., Crewell, S., Dethloff, K., Ebell, K., Lüpkes, C., Macke, A., Notholt, J., Quaas, J., et al.: Understanding causes and effects of rapid warming in the Arctic, Eos, 98, https://doi.org/10.1029/2017EO064803, 2017.

Wild, M., Folini, D., Hakuba, M. Z., Schär, C., Seneviratne, S. I., Kato, S., Rutan, D., Ammann, C., Wood, E. F., and König-Langlo, G.: The energy balance over land and oceans: an assessment based on direct observations and CMIP5 climate models, Climate Dynamics, 44, 3393–3429, https://doi.org/10.1007/s00382-014-2430-z, 2015.

Winkler, P.: The growth of atmospheric aerosol particles as a function of the relative humidity—II. An improved concept of mixed nuclei, Journal of Aerosol Science, 4, 373–387, https://doi.org/https://doi.org/10.1016/0021-8502(73)90027-X, 1973.

Zieger, P., Fierz-Schmidhauser, R., Weingartner, E., and Baltensperger, U.: Effects of relative humidity on aerosol light scattering: results from different European sites, Atmospheric Chemistry and Physics, 13, 10 609–10 631, https://doi.org/10.5194/acp-13-10609-2013, 2013.
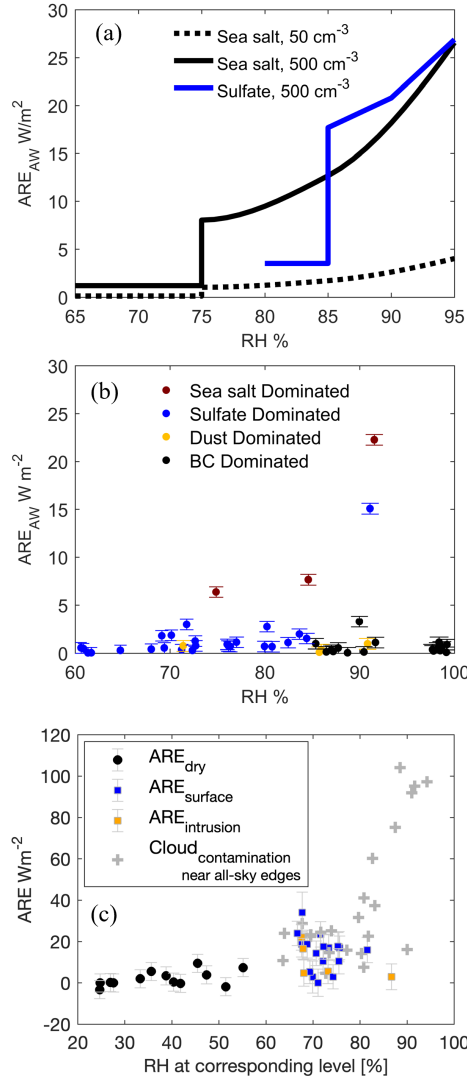
Figure 1. (a) Aerosol Radiation Effect (ARE$_{AW}$) of sea salt (red, black and blue lines) and sulfate (black dotted line) as a function of RH, simulated by LBLDIS with different number density cases; (b) The ARE$_{AW}$ of sea salt(brown), sulfate (blue), dust(yellow) and BC (black) dominant cases measured by emission FTIR (NYAEM-FTS). The aerosol composition retrieval method is given in Sec.4.3 and the methods is given by Ji et al. (2023); (c) ARE under different RH profile scenarios: ARE$_{Dry}$ (black) means that the entire atmosphere is in a dry state (RH < 60%); ARE$_{surface}$ (blue) means that there is a layer of high humidity (RH > 60%) near the ground (< 1 km); ARE$_{intrusion}$ (yellow) represents the situation with a layer of high humidity intrusion (RH > 60%) at high altitude (> 1 km). Gray crosses indicate cloud contamination. The error bars represent one standard deviation of the ARE calculated over a 3-hour period (10:30 - 13:30). Note: ARE$_{AW}$ in this figure (a) refers to simulations and (b) refers to measurements by NYAEM-FTS in the AW region, and ARE in figure c refers to the results of measurements (BSRN) in the mid-infrared range.
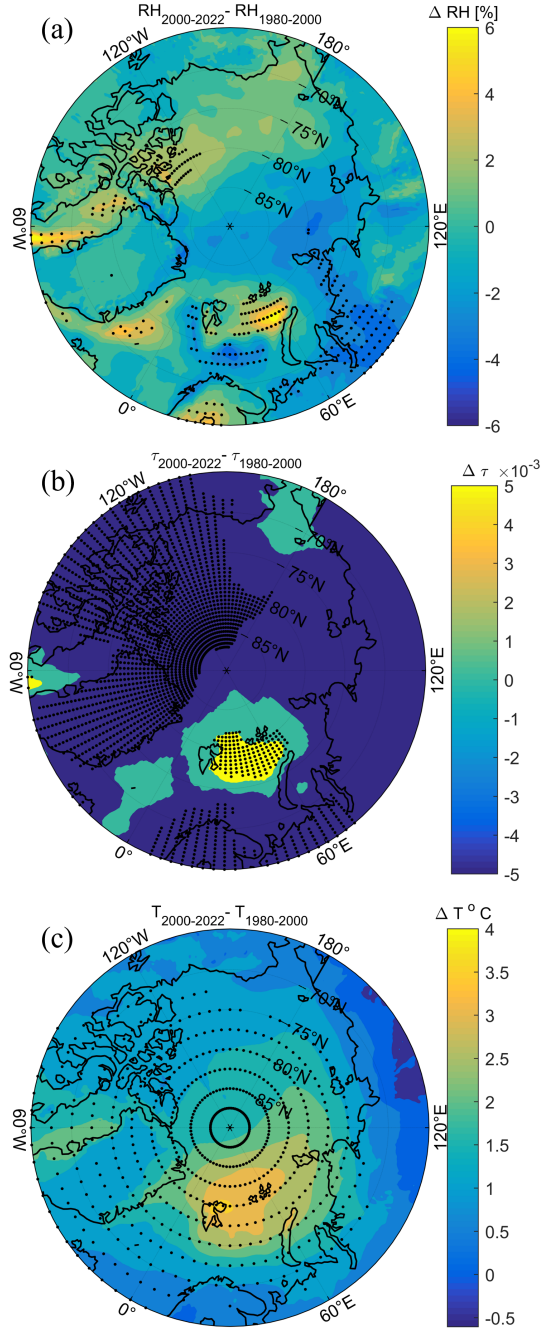
Figure 2. (a) The difference of RH between 2000 - 2022 and 1980 - 2000 in the Arctic at 900 hPa in winter (DJF), data from ERA5 (Hersbach et al., 2023); (b) The difference of Sea salt aerosol optical depth between 2000 - 2022 and 1980 - 2000, data from Merra-2 reanalysis data (Gelaro et al., 2017); (c) The difference of temperature between 2000 - 2022 and 1980 - 2000 in the Arctic at 900 hPa in winter (DJF), data from ERA5 (Hersbach et al., 2023). The black dots in (a), (b), and (c) mean the difference of this grid passes the significance test (95%).
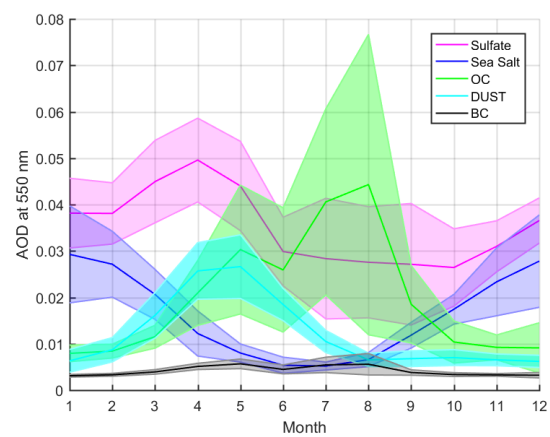
Figure 3. Seasonal variation of sulfate, sea salt, OC, dust and BC from MERRA-2 reanalysis data averaged from 2002 to 2021 with one standard deviation (shaded area) in Ny-Ålesund.
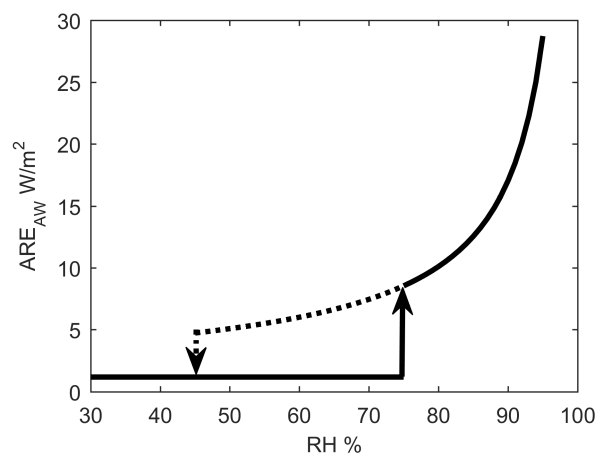
Figure 4. Graph depicting Aerosol Radiative Effects (ARE) as a function of relative humidity (RH), accounting for the deliquescence and efflorescence points. The aerosol component illustrated is sodium chloride, with an aerosol number concentration of 500 particles per cubic centimeter. The deliquescence point is set at 75%, and the efflorescence point is at 46%.

Table 1. Retrieval results (AOD and error) from an aerosol event dominated by sea salt.

Aerosol composition	sea salt	Sulfate	BC	Dust
AOD	0.1125	0.0001	0.0001	0.0128
Error in AOD	0.0013	0.0109	0.0013	0.0070
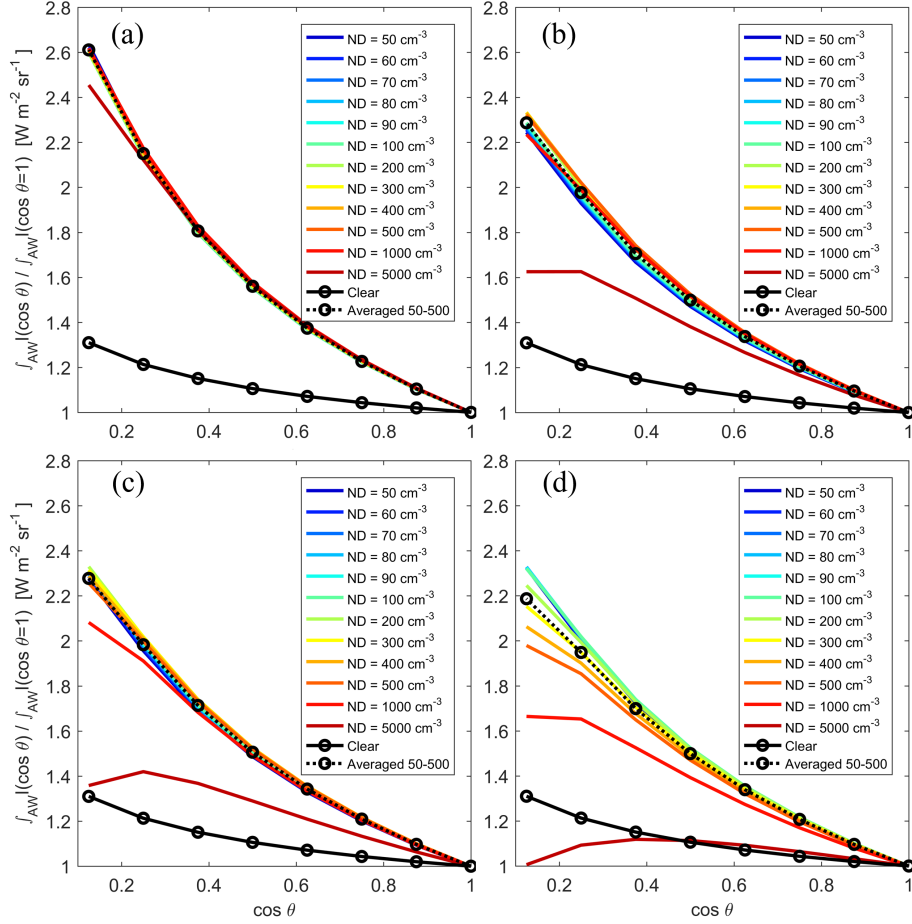
Figure A1. (a)The relationship between Π_{AW} with μ. The varied colors indicate the various number densities of sea salt, while the black line stands for a clear sky scenario. The black dotted lines is the averaged from $50\ \mathrm{cm}^{-3}$ to $500\ \mathrm{cm}^{-3}$. Four cases from the LBLDIS simulation at four RH conditions (65% in (a), 75% in (b), 85% in (c), and 95% in (d)) are provided as well.
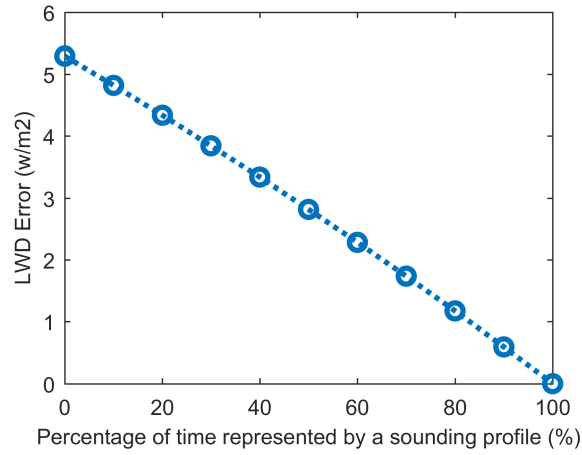
Figure B1. Errors in LWD due to uncertainty in the proportion of time that can be represented by the 90-minute profile over a three-hour period, simulated using the SBDART. The model simulation for Longwave Downward Radiation (LWD) involves changing only the water vapor column content, keeping other atmospheric conditions constant. For example, assuming the profile observations (90 minutes) are representative of only half of the 3-hour period, we consider the scenario: the profile accurately represents the atmospheric state (0.3 gcm^{-2}(Pałm et al., 2010)) for half of the time in Ny-Ålesund, while the other half is characterized by subpolar conditions (0.42 gcm^{-2}, model default). This scenario results in an LWD effect of approximately 2.8 Wm^{-2}.

Table A1. The correction coefficient for atmosphere, sea salt and sulfate at different RH.

RH	<75%	75%	85%	95%
C_Atmos	1.08	1.08	1.08	1.08
C_sea salt	1.40	1.35	1.35	1.35
C_sulfate	1.36	1.36	1.37	1.33